Supplementary information: Dopant-assisted stabilization of negatively charged single nitrogen-vacancy centers in phosphorus-doped diamond at low temperatures

Jianpei Geng,[1,*] Tetyana Shalomayeva,[1,†] Mariia Gryzlova,[1] Amlan Mukherjee,[1] Santo Santonocito,[1] Dzhavid Dzhavadzade,[1] Durga Dasari,[1] Hiromitsu Kato,[2] Rainer Stöhr,[1] Andrej Denisenko,[1] Norikazu Mizuochi,[3,4,5] and Jörg Wrachtrup[1]

[1] *3rd Institute of Physics, ZAQuant, University of Stuttgart, 70569 Stuttgart, Germany*
[2] *National Institute of Advanced Industrial Science and Technology (AIST), Tsukuba, Ibaraki 305-8568, Japan*
[3] *Institute for Chemical Research, Kyoto University, Gokasho, Uji, Kyoto, 611-0011, Japan*
[4] *Center for Spintronics Research Network, Kyoto University, Uji, Kyoto, 611-0011, Japan*
[5] *International Center for Quantum-field Measurement Systems for Studies of the Universe and Particles (QUP), KEK, Tsukuba, Ibaraki 305-0801, Japan*

CONTENTS

EXPERIMENTAL SETUP

The single NV center studies are performed using a high-resolution confocal microscope. An illustration of our home-built confocal microscope is shown in Figure 1. The sample is located inside a Janis ST-500 cold finger Helium flow cryostat at 4 Kelvin. The chamber is evacuated to 10^{-8} mbar. For PL collection we use Nikon LU Plan Fluor 100x air objective (N.A. = 0.9), which is mounted on a NPoint NPXY100Z25 - 102 nanopositioning stage. The emitted photons are detected by Perkin-Elmer avalanche photodiodes (APDs).

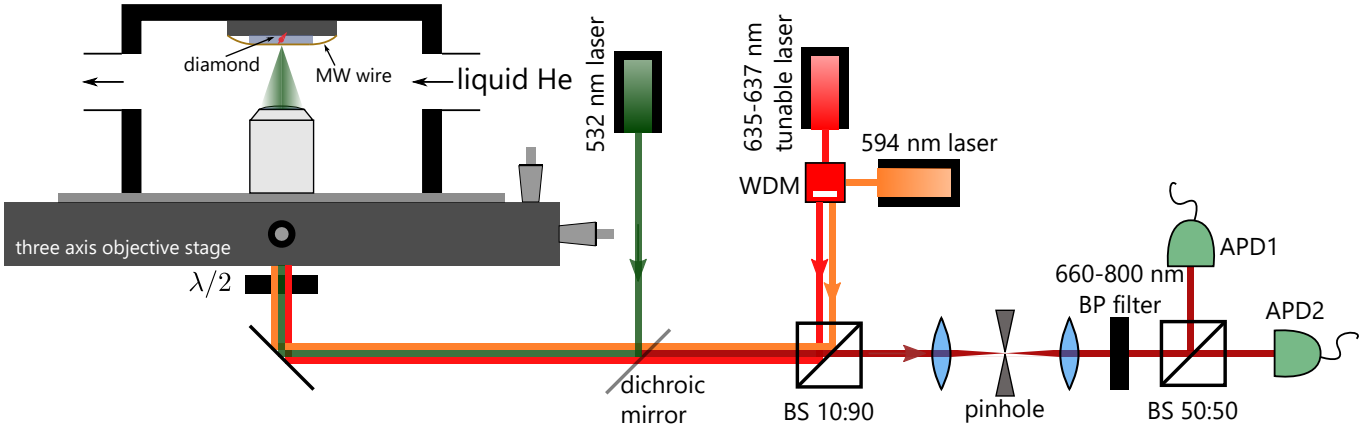

FIG. 1. **Schematic of the experimental setup's optical part**

Three lasers can individually illuminate the sample. The 532 nm excitation is generated by Laser Quantum gem 532, 637 nm resonant excitation is a New Focus Velocity laser TLB-6704, and 594 nm excitation is applied using Cobolt 04-01 Mambo CW diode-pumped laser. The beams of red and orange lasers are combined via 3-Wavelength WDM (RGB Combiner from Thorlabs) and follow the same optical path. Both green and red lasers are pulsed by a double-pass AOM configuration, and the orange excitation is applied in the CW regime. The laser light polarization is adjusted using a half-wave plate from Thorlabs. Its exact angular position is controlled via a motor from LK-Instruments.

The detection path starts with two lenses, which focus the fluorescence beam into a pinhole that blocks out-of-focus light. Afterward, the beam is filtered by a 660-800 nm bandpass filter, split into two via a 50:50 beamsplitter, and reaches the APDs.

The external magnetic field of 67 G along the NV axis orientation is applied by a permanent magnet positioned on top of the cryostat.

SAMPLE PREPARATION

The film of phosphorus-doped diamond was grown by MW plasma-enhanced CVD system as described in [1].

The additional layer of NV centers is created by a 9.8 keV nitrogen ion ($^{15}N^{+}$) implantation with a dose of 1.3×10^{10} atoms per cm^2. Afterward, the diamond is annealed in a high vacuum at 950° for 2 hours and boiled in the 3-acid mixture at 120° for 3 hours. To enhance photon collection efficiency the arrays of nanopillars are etched on the diamond surface [2].

T_2 TIME MEASUREMENTS IN PHOSPHORUS-DOPED DIAMOND

In order to characterize the spin properties and compare them with room temperature results [1] we performed Hahn-echo measurements on different NV centers in the phosphorus-doped diamond. The pulse sequence for these measurements is shown in Figure 2 (a). The spin contrast data points for intrinsic and implanted NV centers are shown in Figure 2 (b) and (c) respectively. The T_2 times are extracted by fitting the data with a stretched exponential function. All the measured coherence times of the intrinsic NV centers in phosphorus-doped diamond are in the range of milliseconds. For the implanted defects this value is two orders of magnitude smaller.

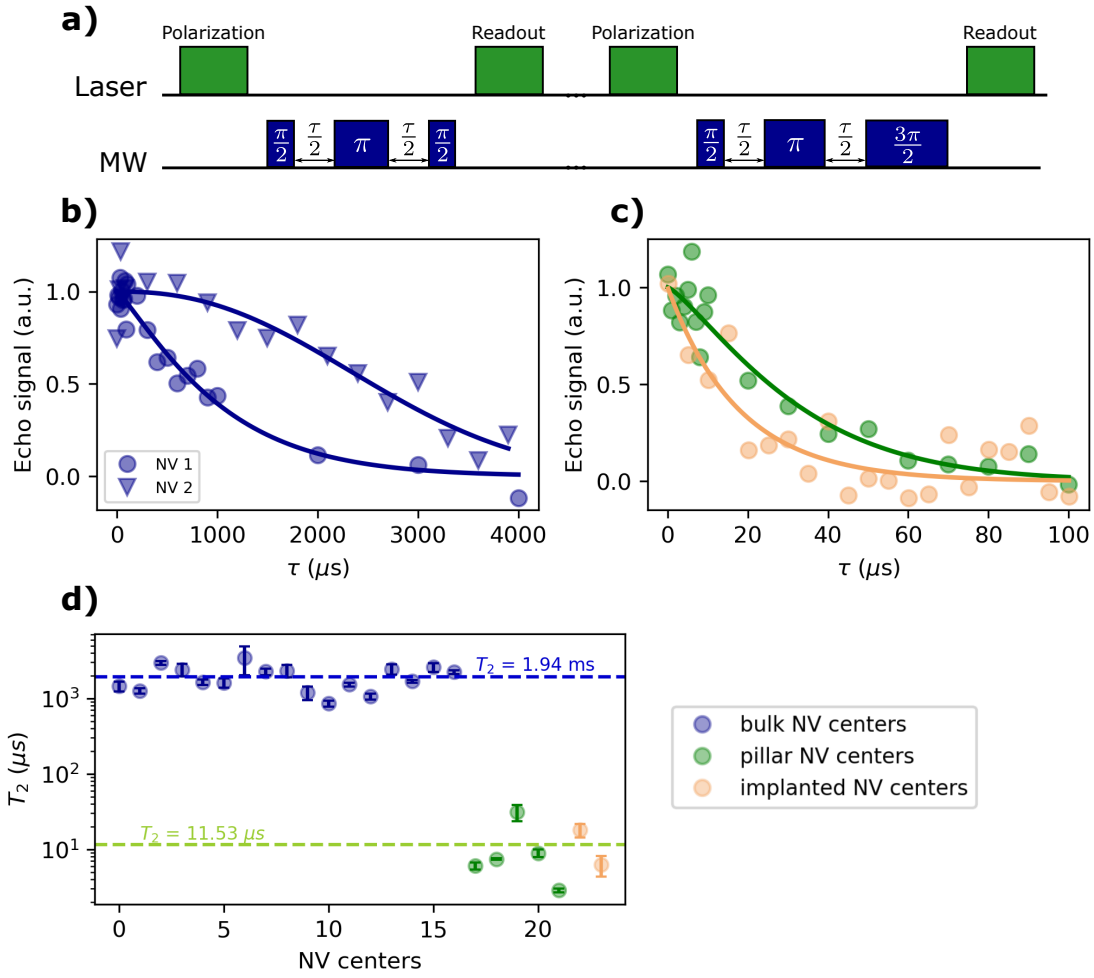

FIG. 2. T_2 **time statistics**

(a) Pulse sequence for Hahn-echo measurements. (b) Echo signal of 2 NV centers, which were created during the growth process (^{14}N isotope impurity). Data are shown by blue circles and triangles (for NV1 and NV2 respectively), and solid lines correspond to the stretched exponential decay fit. (c) Echo signal measured on 2 NV centers created by ^{15}N implantation. Data are shown by green and yellow circles (for NV in the pillars and in non-structured diamond respectively), and solid lines correspond to the stretched exponential decay fit. (d) Statistics of the T_2 time for each observed NV center. The average coherence times are represented by dashed lines.

The detailed statistics of T_2 times of various NV centers in phosphorus-doped diamond are shown in Figure 2(d). These results show the reproducibility of the obtained long coherence times for the centers created during the growth process. The average T_2 time for grown defects is 1.94 ms, and for implanted ones is 11.53 μs. The different local surroundings of each NV center are considered to be the reason for the scatter of T_2 time. The high spin coherence time of point defects in diamond improves magnetic field sensitivity, which is crucial for sensing applications.

STATISTICS OF PLE LINEWIDTH

As mentioned in the main text, PLE spectra of the NV centers created during the growth process show exclusive stability without any repump laser. The ionization and recombination events happen within a single laser detuning sweep. However, stable photoluminescence excitation can be observed at the costs of the broad linewidth of the PLE peaks in order of GHz. The broadening is attributed to the electric field fluctuation caused by the photo-ionization of the phosphorus impurities in the diamond lattice.

Figure 3 (a) shows PLE spectra as a function of excitation laser detuning without additional MW driving, which is fitted with the multi-Lorentz function. In Figure 3 (b) we present the statistics of full width at half maximum (FWHM) of fitted PLE peaks measured on different NV centers in phosphorus-doped diamond. All of them possess broad PLE linewidth in the range of GHz. The average value of fitted FWHM is 2.48 ± 0.19 GHz.

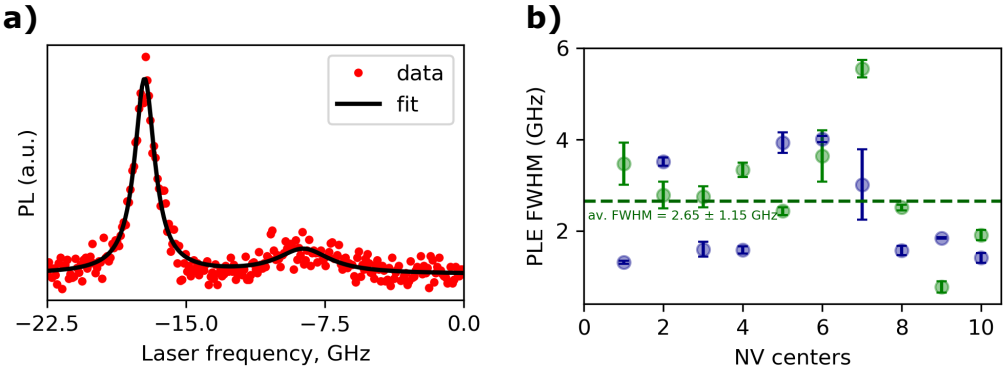

FIG. 3. **PLE FWHM statistics**

(a) PL intensity as a function of laser detuning averaged over the multiple repetitions without MW driving. The detuning is denoted from 636.60 nm excitation wavelength. The circles are experimental data and the solid line represents the fit with a double-Lorentz function. (b) Fitted FWHM of the PLE Lorentzian distributions for every examined NV center measured at the same experimental conditions. The average value of FWHM is 2.48 ± 0.19 GHz. Green and dark blue colors represent the widths of two PLE peaks for each defect.

LASER POWER DEPENDENCE OF PLE SPECTRA

In addition, we examine the red laser power dependence of the PLE spectra of the NV center created during the diamond CVD growth process. The recorded spectra with the excitation powers ranging from 23 nW to 860 nW are shown in Figure 4 (a). The laser frequency represents the detuning from a frequency corresponding to 636.6 nm. PLE peaks show exceptional long-term spectral stability independently of the laser power. The PLE spectra are fitted with a multi-Lorentz function

$$I_{\mathrm{PL}} = I_{\mathrm{bg}} + \sum_i \frac{A_i}{(\nu - \nu_{0,i})^2 + (\Gamma_i/2)^2}, \tag{1}$$

where I_{PL} is the PL intensity as a function of laser frequency ν, I_{bg} is the background PL intensity, A_i, $\nu_{0,i}$, and Γ_i are the amplitude, resonant frequency, and linewidth for the i-th peak. The fits are shown as solid lines in Figure 4 (a). Figures 4 (b) and (c) show the extracted linewidth Γ_i and amplitude A_i from the fit as a function of the laser power.

In order to understand the laser power dependence of the PLE linewidths and amplitudes, we consider the steady-state solution of the optical Bloch equations describing a two-level system. The PL intensity I_{PL} is proportional to the steady-state population P_{exc} of the excited state [3]

$$I_{\mathrm{PL}} \propto P_{\mathrm{exc}} = \frac{1}{2} \frac{\Omega^2 T_1/T_2}{[2\pi(\nu - \nu_0)]^2 + T_2^{-2} + \Omega^2 T_1/T_2}, \tag{2}$$

where ν is the laser frequency, ν_0 is the resonant frequency of the two-level system, T_1 and T_2 are the relaxation and coherence time, and

$$\Omega = c\sqrt{P_{\mathrm{L}}} \tag{3}$$

is the Rabi frequency with P_{L} being the laser power and c a coefficient.

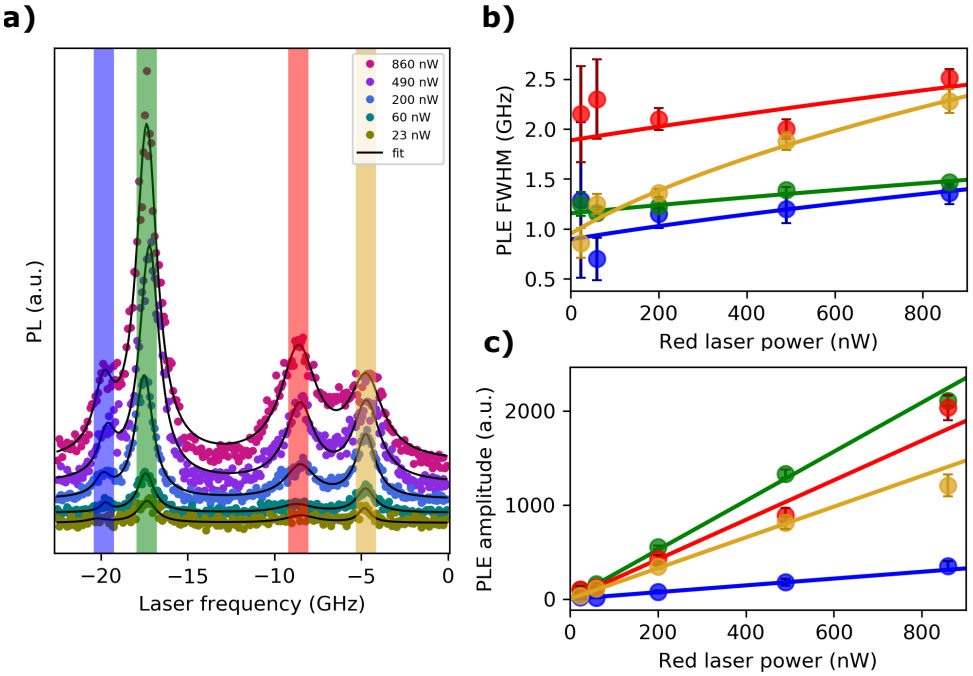

FIG. 4. **PLE laser power dependence**

(a) PLE spectra detuned from 636.6 nm at different red laser powers (23, 60, 200, 490, and 860 nW). The circles are experimental data and the solid line is fit with a multi-Lorentz function. Blue, green, red, and yellow marked regions correspond to 4 different observed peaks. (b) Resonant laser power dependence of PLE full width at half maximum (FWHM). Colors represent the FWHM values for each peak in (a) respectively. The solid lines are fit. (c) Resonant laser power dependence of PLE amplitude. Colors represent the amplitude values for each peak in (a) respectively. The solid lines are fit.

By substituting Equation 3 into Equation 2 and comparing it to Equation 1, one could obtain

$$\begin{aligned} A_i &\propto c_i^2 \frac{T_{1,i}}{T_{2,i}} P_{\mathrm{L}}, \\ \Gamma_i &= \frac{1}{\pi T_{2,i}} \sqrt{1 + c_i^2 T_{1,i} T_{2,i} P_{\mathrm{L}}}, \end{aligned} \tag{4}$$

where c_i, $T_{1,i}$, and $T_{2,i}$ are the coefficient c, relaxation time T_1, and coherence time T_2 for the i-th peak of the PLE spectra. Some of them (e.g. $T_{1,i}$) may be the same for all the peaks. However, whether it's the same or different for each peak is not the focus of our discussion. Equation 4 gives the laser power dependence of the PLE amplitude and linewidth if c_i, $T_{1,i}$, and $T_{2,i}$ are independent of the laser power P_{L}. Especially, the derived PLE amplitude A_i shows a linear laser power dependence.

We fit the PLE linewidth and amplitude extracted from the experimental spectra with Equation 4 assuming that c_i, $T_{1,i}$, and $T_{2,i}$ are constant. The fits are shown as solid lines in Figure 4 (b) and (c). The good agreement between the fit and data indicates that $T_{2,i}$ is independent of the laser power in the applied power range. The fit of the PLE linewidth gives a zero-power-limit linewidth $1/(\pi T_{2,i})$ in order of 1 GHz for all the peaks, which is much larger than the Fourier transform limited linewidth of NV centers in intrinsic diamond [4]. The broader linewidth and corresponding shorter coherence time $T_{2,i}$ could be attributed to charge fluctuation caused by the photo-ionization of phosphorus impurities. The photo-ionization process leads to a time-varying charge state of the phosphorus impurity, which could cause a fluctuating electric field on the NV center and shorten the NV coherence time due to the Stark effect. The fit to the PLE linewidth indicates that this broadening effect is significant ($\sim$ 1 GHz) but keeps almost constant in our applied laser power range. We try to understand this counterintuitive phenomenon by considering the screening effect of the photo-ionized free electrons on the electric field created by the photo-ionized phosphorus impurities in the next section.

SCREENING EFFECT OF ELECTRONS ON THE ELECTRIC FIELD CREATED BY PHOTO-IONIZED PHOSPHORUS

Here we consider the screening effect of electrons created by photo-ionization of phosphorus impurities and show that it could lead to an electric field from the phosphorus impurity insensitive to laser power P_{L} in a certain power range. For simplicity, we assume that the electrons are homogeneously distributed in space with a density n_{e} equal to the density of ionized phosphorus impurities $n_{\mathrm{P,\ ion}}$. The experimental linear laser power dependence of recombination rate indicates that the electron density is proportional to P_{L} in the power range. Therefore, we use the electron density n_{e} as a representation of the laser power P_{L} in the calculation. The existence of electrons could screen the electric field created by the ionized phosphorus impurity, leading to a modified electric potential [5, 6]

$$\phi(r) = \frac{Q}{4\pi\varepsilon_0\varepsilon_r r} e^{-k_0 r}, \tag{5}$$

where $\phi(r)$ is the electric potential at a distance r from the ionized phosphorus impurity, Q is the charge, ε_0 is the vacuum permittivity, ε_r is the relative permittivity of diamond, and k_0 is the screening wave vector. The magnitude of the electric field could be calculated as

$$E = \frac{Q}{4\pi\varepsilon_0\varepsilon_r r^2} e^{-k_0 r}(1 + k_0 r). \tag{6}$$

Compared to the electric field without the screening effect, the electric field is multiplied by an additional factor

$$f(k_0 r) = e^{-k_0 r}(1 + k_0 r). \tag{7}$$

The factor $f(k_0 r)$ is always smaller than 1 for arbitrary positive $k_0 r$ and decreases with increasing $k_0 r$.

We estimate the screening wave vector with the Thomas-Fermi approximation [6]. The screening wave vector k_0 could be calculated as

$$k_0 = \sqrt{\frac{m e^2 k_{\mathrm{F}}}{\varepsilon_0\varepsilon_r \pi^2 \hbar^2}}, \tag{8}$$

where m is the effective electron mass, e is the electron charge, $\hbar$ is the reduced Plank constant, and k_{F} is the Fermi wavevector which is related to the electron density by

$$n_{\mathrm{e}} = 2\frac{1}{(2\pi)^3}\left(\frac{4}{3}\pi k_{\mathrm{F}}^3\right). \tag{9}$$

Combining Equation 8 and Equation 9 gives

$$k_0 = \frac{e}{\pi\hbar}\left(\frac{m}{\varepsilon_0\varepsilon_r}\right)^{\frac{1}{2}}\left(3\pi^2 n_{\mathrm{e}}\right)^{\frac{1}{6}}, \tag{10}$$

which enables us to estimate the screening wave vector k_0 and screening length $1/k_0$ as a function of the electron density n_{e}. Figure 5 (a) shows the calculated screening length when the effective electron mass m takes the value of the electron rest mass m_0, the longitudinal effective mass $m_{\parallel} = 1.5m_0$, the transversal effective mass $m_{\perp} = 0.341m_0$, and the effective Hall mobility mass $m_H = (2m_{\parallel} + m_{\perp})/(2 + m_{\parallel}/m_{\perp})$, respectively [7].

The electric field created by ionized phosphorus impurities in a unit volume could be calculated with Equation 6 and Equation 10 by substituting Q with the density of ionized phosphorus impurities $n_{\mathrm{P,\ ion}} = n_{\mathrm{e}}$,

$$E_{\mathrm{perV}} = \frac{n_{\mathrm{e}}}{4\pi\varepsilon_0\varepsilon_r r^2} e^{-k_0 r}(1 + k_0 r). \tag{11}$$

Since k_0 scales as $n_{\mathrm{e}}^{1/6}$, the factor $f(k_0 r)$ decreases with increasing n_{e}. On the other hand, E_{perV} increases with n_{e} if neglecting the factor $f(k_0 r)$. Therefore, if $k_0 r \ll 1$, the screening effect is negligible and the electric field increases linearly with the electron density n_{e}; if $k_0 r \gg 1$, the screening effect dominates and the electric field decreases exponentially with n_{e}. Such a conclusion is intuitively natural, since increasing laser power leads to an increase of the ionization probability of phosphorus impurities, which on one hand increases the electric field by increasing the density of ionized phosphorus impurity, on the other hand, decreases the electric field by enhancing the screening effect with increased electron density. Such a competition mechanism leads to the electric field reaching a maximum at a certain

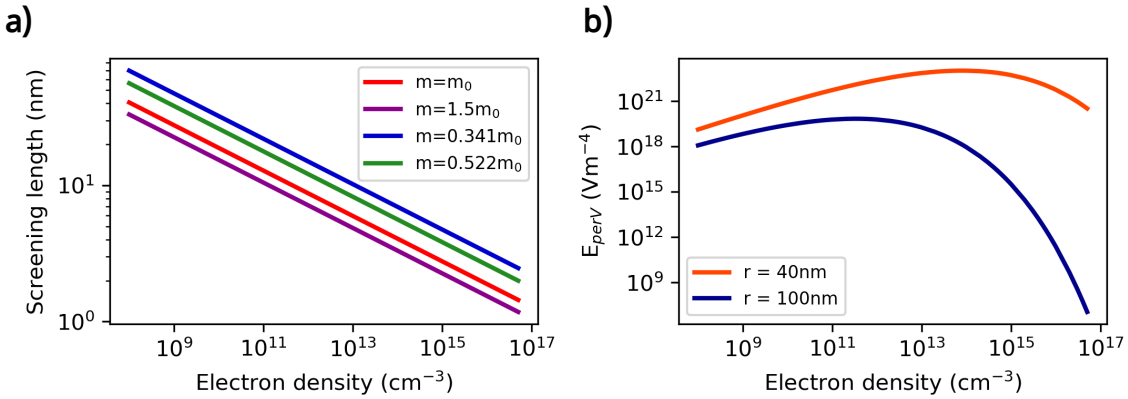

FIG. 5. **Calculation of electric field created by ionized phosphorus impurities considering screening effect** (a) Screening length as a function of electron density for various effective electron mass m. m_0 is the electron rest mass. (b) Electric field created by ionized phosphorus impurities in a unit volume as a function of electron density.

electron density n_{e} (corresponding to a certain laser power P_{L}). We expect that the electric field is insensitive to the electron density n_{e} and laser power P_{L} near the maximum. Figure 5 (b) shows the calculated electric field created by ionized phosphorus impurities in a unit volume E_{perV} at a distance of $r = 40$ nm and $r = 100$ nm. As expected the electric field remains almost unchanged near the maximum even if the electron density changes by 2 orders. Since the electric field created by ionized phosphorus impurities could be insensitive to the laser power in a certain power range, similar behavior of electric field fluctuation could be expected.

LASER POLARIZATION DEPENDENCE OF PLE SPECTRA

The polarization of the resonant excitation light can be varied by using a half-wave plate installed in the optical path. By adjusting the rotation angle of $\lambda/2$ plate the efficiency of resonant excitation of optical transitions in the PLE spectrum can be changed. The experimentally obtained normalized PLE spectra with the red laser polarization ranging from 20° to 200° are shown as the grid in Figure 6 (a).

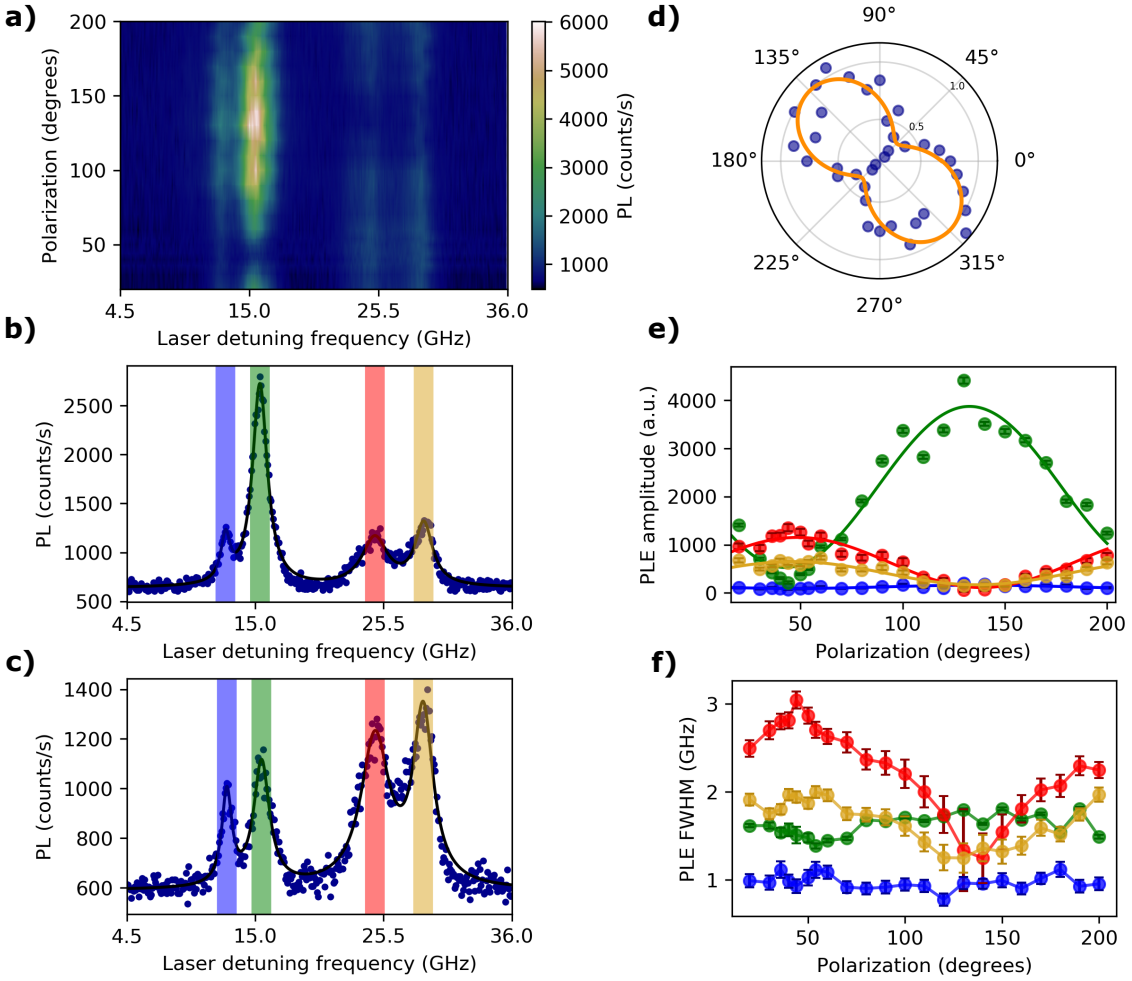

FIG. 6. **PLE laser polarization dependence**

(a) Normalized PL intensity as a function of laser detuning (detuned from 636.50 nm) for different laser polarization values in the range of 20° - 200 °. (b) and (c) PLE spectra at 70° and 40° laser polarization respectively. The circles are experimental data and the solid line is a fit with the multi-Lorentz function. (d) Normalized PL intensity dependence on the laser polarization. The excitation wavelength is 636.50 nm and the detuning is 15.5 GHz. (e) Laser polarization dependence of the PLE amplitude. The periodic fit is represented by a solid line. (f) Laser polarization dependence of the PLE full width at half maximum (FWHM). Colors in (e) and (f) correspond to the individual PLE peaks marked in (b) and (c).

The PLE spectra obtained with 70° and 40° excitation polarization are shown in Figure 6 (b) and (c) respectively. The detuning frequencies of the peaks are stable and independent of the resonant excitation polarization. However, the amplitudes vary resulting in different optical excitation efficiency of certain transitions. For example, the normalized amplitude of the peak at 15.5 GHz detuning for different laser polarizations is shown in Figure 6 (d) in polar coordinates.

The spectra are fitted with a multi-peak Lorentzian function. The parameters extracted from the fit are presented in Figures 6 (e) and (f) as a function of excitation polarization. The colors there correspond to the marked peaks in (b) and (c). The PLE amplitude changes as a cosine function for each peak as shown in Figure 6 (e). The corresponding linewidth of the transitions in (f) periodically changes in phase with the amplitude.

EXTRACTING THE NV IONIZATION AND RECOMBINATION RATES FROM THE TIME TRACES OF FLUORESCENCE

The NV charge state is real-time monitored by recording the fluorescence under the illumination of 636 nm resonant excitation or 594 nm orange laser. The experiments are performed at liquid helium temperature. Since the excitation is far red-detuned from the excitation of NV^0 and phonon is largely suppressed at this temperature, the excitation of NV^0 is negligible and only NV^- is excited. Therefore, detectable fluorescence from the NV center is possible only when it is in the NV^- charge state. When in NV^0 charge state, a much lower fluorescence intensity regarding the background is observed. Figure 7 (a) shows an example of the time trace of fluorescence. The time trace is recorded by collecting photon counts into $\tau_0 = 10$ ms bins for 50 s under the illumination of 148 nW, 636 nm resonant excitation.

The NV ionization and recombination rates could be extracted from the photon counts distribution [8, 9]. It is assumed that the photon counts distribution could be fully described by 4 rates: the NV ionization rate k_{ion}, recombination rate k_{rec}, and the photon count rates γ_- and γ_0 when in NV^- and NV^0, respectively. This assumption is a good approximation when the NV photo-dynamics is much faster than the charge dynamics and holds for all our measurements. The photon count distribution could be described as

$$P(n;\tau) = P(n;\tau|NV^-)P(NV^-) + P(n;\tau|NV^0)P(NV^0), \tag{12}$$

where $P(n;\tau)$ is the probability to have n photon counts in a bin of time duration τ, $P(n;\tau|NV^k)$ ($k \in \{-,0\}$) is the probability in the condition that NV is initially in NV^k charge state, and $P(NV^k)$ is the probability of NV being in NV^k. Since the time trace is recorded under continuous excitation, a steady-state probability is considered

$$\begin{aligned} P(NV^-) &= \frac{k_{\text{rec}}}{k_{\text{ion}} + k_{\text{rec}}}, \\ P(NV^0) &= \frac{k_{\text{ion}}}{k_{\text{ion}} + k_{\text{rec}}}. \end{aligned} \tag{13}$$

Considering the charge state switching during τ, the probability $P(n;\tau|NV^-)$ and $P(n;\tau|NV^0)$ could be calculated as

$$\begin{aligned} P(n;\tau|NV^-) &= P(n;\tau|NV^-,\text{even}) + P(n;\tau|NV^-,\text{odd}), \\ P(n;\tau|NV^0) &= P(n;\tau|NV^0,\text{even}) + P(n;\tau|NV^0,\text{odd}), \end{aligned} \tag{14}$$

where $P(n;\tau|NV^k,\text{even})$ and $P(n;\tau|NV^k,\text{odd})$ ($k \in \{-,0\}$) is the probability in the condition that there are even and odd numbers of charge state switching during τ, respectively. The expression for $P(n;\tau|NV^k,\text{even})$ and $P(n;\tau|NV^k,\text{odd})$ has been derived [8] as

$$\begin{aligned} P(n;\tau|NV^-,\text{even}) &= \int_0^\tau dt \sqrt{\frac{k_{\text{ion}}k_{\text{rec}}t}{\tau-t}} e^{(k_{\text{rec}}-k_{\text{ion}})t - k_{\text{rec}}\tau} I_1(2\sqrt{k_{\text{ion}}k_{\text{rec}}t(\tau-t)})\text{Po}(n;\gamma_- t + \gamma_0(\tau-t)) + e^{-k_{\text{ion}}\tau}\text{Po}(n;\gamma_-\tau), \\ P(n;\tau|NV^-,\text{odd}) &= \int_0^\tau dt k_{\text{ion}} e^{(k_{\text{rec}}-k_{\text{ion}})t - k_{\text{rec}}\tau} I_0(2\sqrt{k_{\text{ion}}k_{\text{rec}}t(\tau-t)})\text{Po}(n;\gamma_- t + \gamma_0(\tau-t)), \\ P(n;\tau|NV^0,\text{even}) &= \int_0^\tau dt \sqrt{\frac{k_{\text{ion}}k_{\text{rec}}t}{\tau-t}} e^{(k_{\text{ion}}-k_{\text{rec}})t - k_{\text{ion}}\tau} I_1(2\sqrt{k_{\text{ion}}k_{\text{rec}}t(\tau-t)})\text{Po}(n;\gamma_0 t + \gamma_-(\tau-t)) + e^{-k_{\text{rec}}\tau}\text{Po}(n;\gamma_0\tau), \\ P(n;\tau|NV^0,\text{odd}) &= \int_0^\tau dt k_{\text{rec}} e^{(k_{\text{ion}}-k_{\text{rec}})t - k_{\text{ion}}\tau} I_0(2\sqrt{k_{\text{ion}}k_{\text{rec}}t(\tau-t)})\text{Po}(n;\gamma_0 t + \gamma_-(\tau-t)), \end{aligned} \tag{15}$$

where $I_0(x)$ and $I_1(x)$ are the modified Bessel functions of the first kind, and $\text{Po}(n;x)$ is the Poisson distribution function representing the probability to have n photon counts with average counts of x.

The photon count distribution corresponding to $\tau = n_{\text{bin}}\tau_0$ for an integer n_{bin} could be obtained from the experimental time trace. By fitting the photon count distribution with Equations 12-15, the ionization rate k_{ion} and recombination rate k_{rec} could be extracted. Figure 7 (b) shows the photon count distribution from the time trace shown in Figure 7 (a) with $n_{\text{bin}} = 1$. The fit shown as the solid line gives $k_{\text{ion}} = 1.6 \pm 2.0$ s^{-1} and $k_{\text{rec}} = 35 \pm 43$ s^{-1}. While it fits the photon count distribution well, the uncertainty of the extracted rates is large. Essentially the precision of the fitting parameters k_{ion} and k_{rec} depends on the selection of $\tau = n_{\text{bin}}\tau_0$: τ needs to be large enough to ensure sufficient charge state switching to occur, and small enough to avoid reaching a steady state. Generally

$\tau \sim 1/(k_{\rm ion} + k_{\rm rec})$ is selected for better precision [8]. We calculate the photon count distributions with various $n_{\rm bin}$ and fit each of them. The extracted $k_{\rm ion}$ and $k_{\rm rec}$ with uncertainties are shown as the blue-filled circles with error bars in Figure 7 (c) and (d). While the differences in the rates for various $n_{\rm bin}$ are within the uncertainties, the uncertainties show a clear $n_{\rm bin}$ dependence.

To further optimize the precision of the rates $k_{\rm ion}$ and $k_{\rm rec}$, we assemble the photon count distributions with various $n_{\rm bin}$ into two-dimensional data and consider it as a function of both photon count n and τ. The two-dimensional data is fitted with Equations 12-15. This enables us to fit all the photon count distributions with unique values of $k_{\rm ion}$, $k_{\rm rec}$, γ_-, and γ_0. The extracted $k_{\rm ion}$ and $k_{\rm rec}$ with uncertainty are shown as the red filled circle with an error bar in Figure 7 (c) and (d), respectively. The uncertainties of the rates with this method are much smaller than those by fitting each photon count distribution corresponding to a single individual $n_{\rm bin}$.

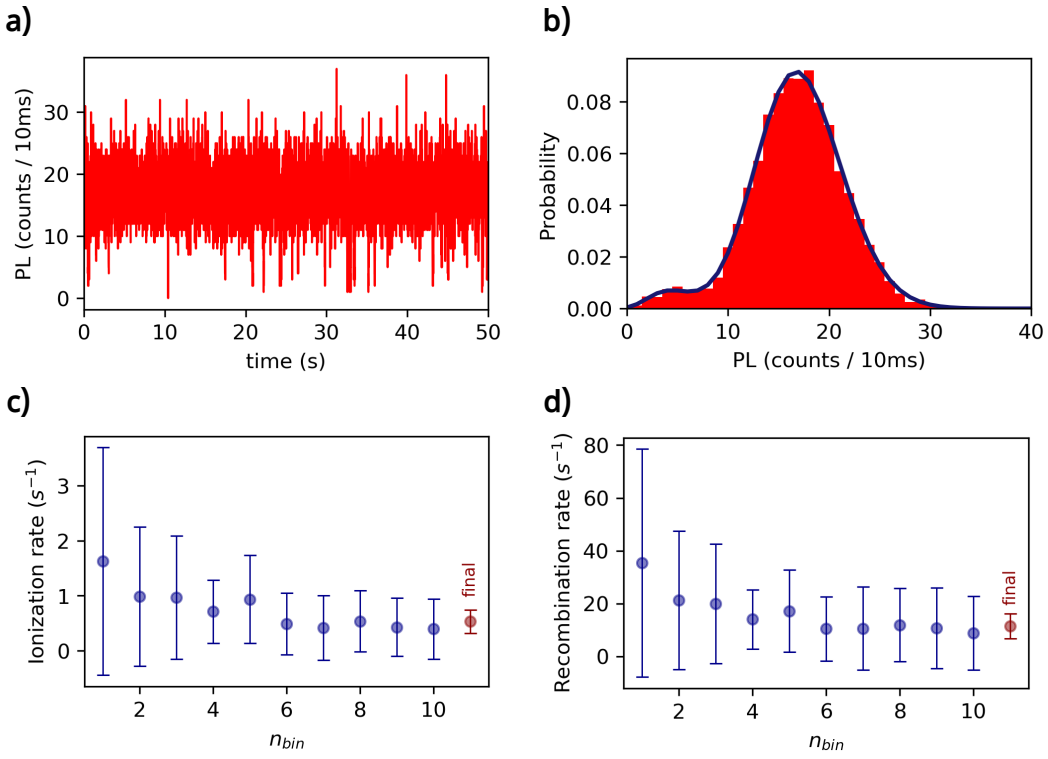

FIG. 7. **Extraction of ionization and recombination rates from the time trace of fluorescence**

(a) An example of the time trace of fluorescence. The time trace is recorded by collecting photon counts into $\tau_0 = 10$ ms bins for 50 s under the illumination of 148 nW, 636 nm resonant excitation. (b) Photon count distribution corresponding to $\tau = \tau_0$ from the time trace shown in (a). The blue solid line is the fit with Equations 12-15 in the text. (c) Extracted ionization rates by fitting the photon count distributions with Equations 12-15 in the text. The blue-filled circles show the results by fitting each individual photon count distribution corresponding to $\tau = n_{\rm bin}\tau_0$ for various $n_{\rm bin}$. The red-filled circle is the result of fitting all the photon count distributions as two-dimensional data. Error bars show the 95% confidence interval. (d) Same as (c), but for the extracted recombination rates.

LASER POWER DEPENDENCE OF RECOMBINATION RATE FOR VARIOUS NVS

We checked the laser power dependence of the recombination rate of various NV centers. The results are shown in Figure 8. All the investigated NV centers show a linear laser power dependence of recombination rate.

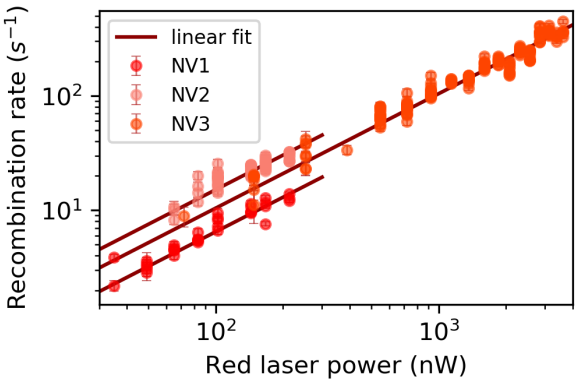

FIG. 8. **Laser power dependence of the recombination rate of various NV centers.** The filled circles are experimental data (extracted recombination rates by fitting the photon count distributions from experimental time traces of fluorescence at various laser powers) and the solid lines are linear fits.

NV^- CHARGE STATE POPULATION

Recently the exclusive negatively charged state of the NV centers in phosphorus-doped diamond was shown at room temperature [10]. Generating a pure NV^- charge state is of big importance for quantum information applications leading to a high-fidelity operation. Phosphorus impurities in an n-doped diamond can donate electrons to NV^0 thereby changing its state to NV^-. In order to check the NV^- population of the centers in phosphorus-doped diamond we optically excited them with red and orange lasers for bulk and implanted defects respectively. The time traces are recorded at different laser powers. The histograms of the observed fluorescence time traces are shown in Figures 9 (a) and (b).

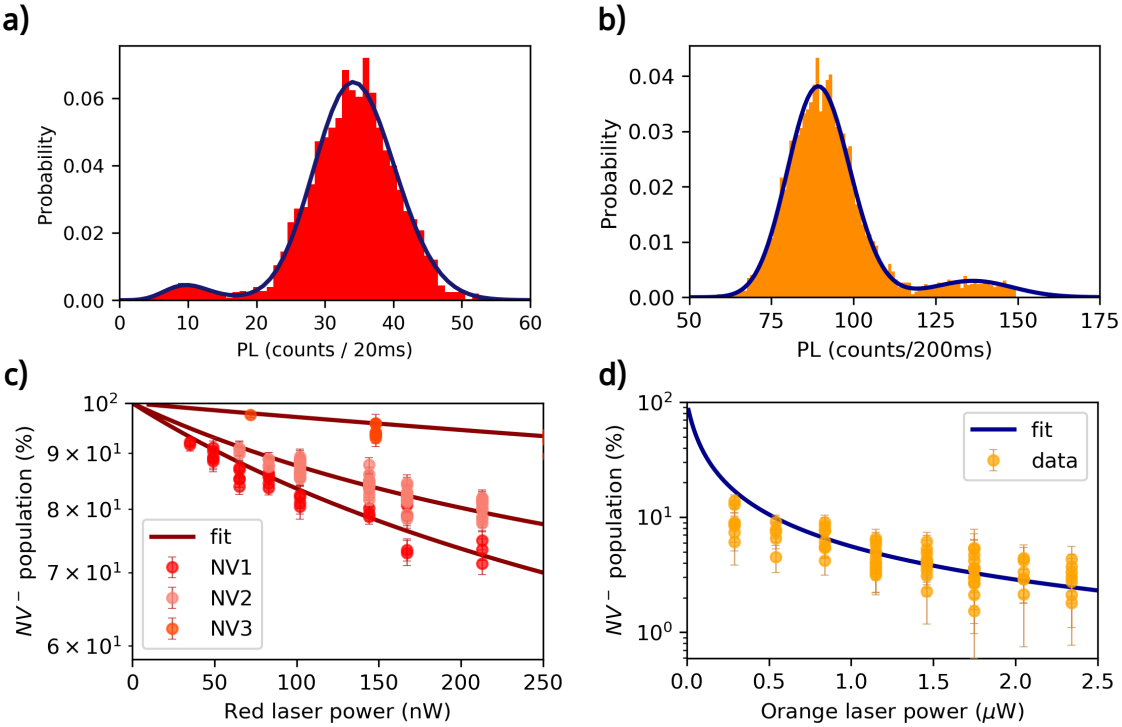

FIG. 9. NV^- **charge state population statistics**

(a) The histogram of the fluorescence time trace under CW illumination of 148 nW resonant 636 nm laser for the bulk NV center. The solid line is a fit. The histogram shows a large probability of a higher count rate, corresponding to the dominating NV^- charge state. (b) The implanted defect's histogram of the fluorescence time trace under CW illumination of 290 nW 594 nm orange laser. The observation of the low count rate has a higher probability, indicating the NV^0 charge state superiority. The solid line shows the distribution fit. (c) NV^- charge state population as a function of excitation laser power for three defects in the bulk diamond. The fit is shown with solid lines. (d) The population of NV^- charge state for different orange laser powers of an implanted defect. The fit is represented by a solid line. In (c) and (d) vertical axis is shown in the logarithmic scale.

By repeating the time trace recording for different excitation powers and analyzing the corresponding histograms the population of NV^- charge state is extracted. Its dependencies on the excitation laser power for intrinsic and implanted NV centers are shown in Fugures 9 (c) and (d) respectively. The grown defects in the bulk phosphorus-doped diamond possess the NV^- charge state population close to 100%, however, the implanted Nv centers are only up to 10% of the time in the negative charge state. This observation shows the improvement of the charge state stability for the grown defects in phosphorus-doped diamond at cryogenic conditions.

CHARGE INITIALIZATION

For further investigation of charge state dynamics of the implanted NV centers in phosphorus-doped diamond, the charge initialization experiments are performed. There, the defect is optically excited with the green laser pulse of variable duration τ. Afterward, the fluorescence of the NV center is recorded for 10 ms, while the orange illumination with the power 7.2 μW is still applied. The obtained photoluminescence is normalized and fitted with the exponentially rising function as shown in Figure 10 (a). The decay constant of the fitting function gives the sum of ionization and recombination rates $k_{ion} + k_{rec} = 0.047 \pm 0.007\,\mu s^{-1}$ for 43 μW green laser pulse excitation.

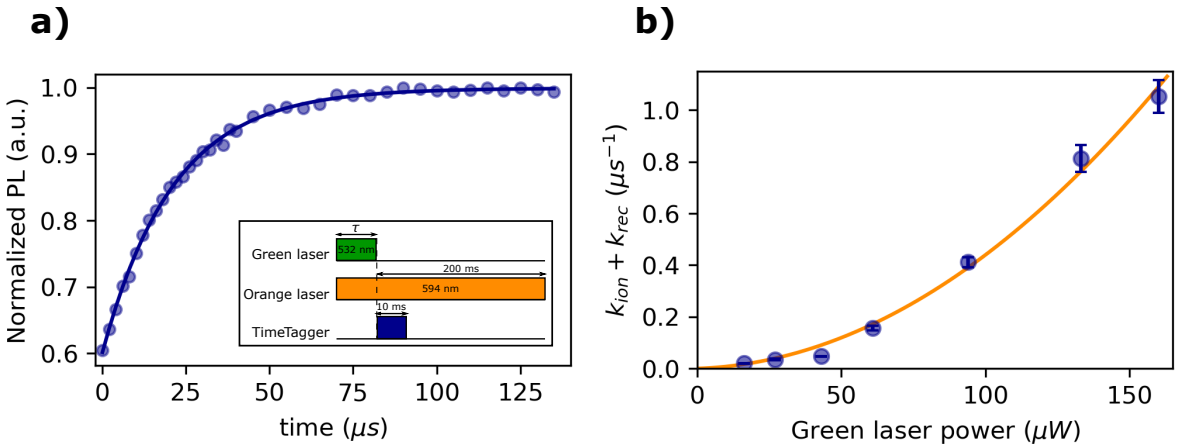

FIG. 10. **Charge initialization**

(a) The initialization of the charge state with the 532 nm green laser pulse of variable duration τ. The photoluminescence is measured for 10 ms after the green laser pulse. Orange laser is applied in the CW mode with the power of 7.2 μW. The inset shows the applied pulse sequence. (b) Green laser power dependence of the sum of ionization and recombination rates. A solid line is a fit with a quadratic function.

The measurements are repeated for several green laser powers aiming to obtain the laser power dependency of the sum of ionization and recombination rates in Figure 10 (b). The plot is fitted with a parabola showing the quadratic dependency on the initialization laser power.

CHARGE READOUT

In order to examine the charge state of the implanted defects under the continuous wave orange laser illumination the following pulse sequence is applied. First, the green laser pulse (50 μW, 20 ms duration) excites the defect to the NV^- charge state. Subsequently, the emitted photons are collected under the CW illumination of 3.5 μW orange laser. The applied pulse sequence is shown in the inset. The observed fluorescence decay caused by charge state switching is presented in Figure 11 (a) and is fitted with an exponential function. The decay constant gives the sum of the ionization and recombination rates of $k_{ion} + k_{rec} = 26.38 \pm 1.15 s^{-1}$ during the charge state readout process.

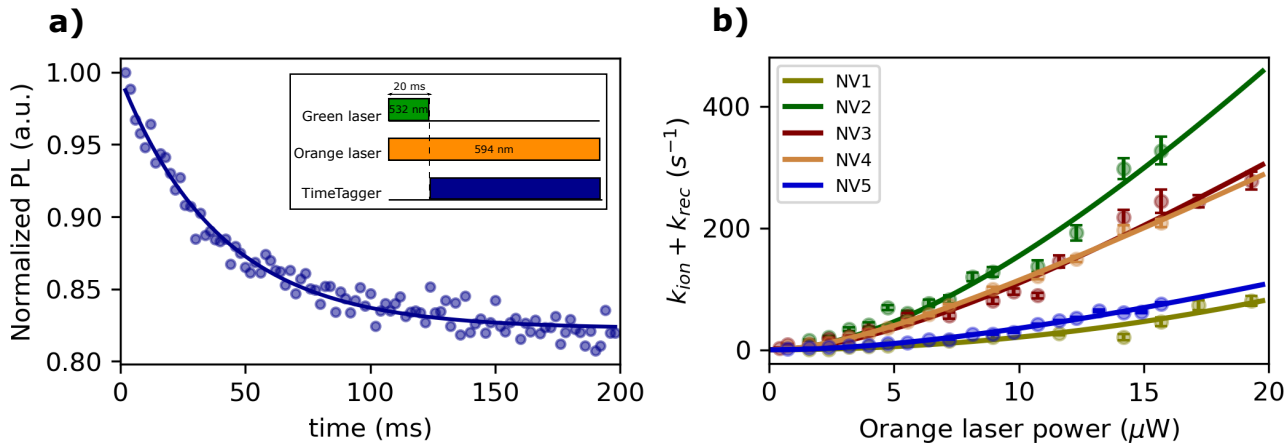

FIG. 11. **Charge readout**

(a) An exponential decay of photoluminescence after 20 ms green laser pulse under continuous illumination with 3.5 μW, 594 nm orange laser. The circles represent experimental data and the solid line is a fit. The inset shows the applied pulse sequence. (b) Orange laser power dependence of the charge dynamics rate for different NV centers. The circles represent the rates extracted from (a), and the solid line is a fit with a saturation-modified quadratic function.

The measurements are repeated for different 594 nm readout laser powers and fitted with the exponential decay. The obtained laser power dependencies of the sum of ionization and recombination rates during charge state readout are presented for five defects in Figure 11 (b). The extracted values are fitted with a saturation-modified parabola indicating the quadratic dependency on the readout laser power.

* jianpei.geng@pi3.uni-stuttgart.de; These authors contributed equally.
† tetyana.shalomayeva@pi3.uni-stuttgart.de; These authors contributed equally.

[1] E. Herbschleb, H. Kato, Y. Maruyama, T. Danjo, T. Makino, S. Yamasaki, I. Ohki, K. Hayashi, H. Morishita, M. Fujiwara, *et al.*, Nature Communications **10**, 3766 (2019).
[2] S. A. Momenzadeh, R. J. Stohr, F. F. De Oliveira, A. Brunner, A. Denisenko, S. Yang, F. Reinhard, and J. Wrachtrup, Nano letters **15**, 165 (2015).
[3] E. B. Flagg, A. Muller, J. Robertson, S. Founta, D. Deppe, M. Xiao, W. Ma, G. Salamo, and C.-K. Shih, Nature Physics **5**, 203 (2009).
[4] P. Tamarat, T. Gaebel, J. R. Rabeau, M. Khan, A. D. Greentree, H. Wilson, L. C. L. Hollenberg, S. Prawer, P. Hemmer, F. Jelezko, and J. Wrachtrup, Physical Review Letters **97**, 083002 (2006).
[5] P. Debye and E. Hückel, Physikalische Zeitschrift **24**, 185 (1923).
[6] N. W. Ashcroft and N. D. Mermin, *Solid State Physics* (Thomson Learning, Toronto, 1976).
[7] C. E. Nebel, in *Nanodiamonds, Advanced Material Analysis, Properties and Applications*, edited by J.-C. Arnault (Elsevier ISBN: 978-0-323-43029-6, 2017) pp. 1–24.
[8] B. J. Shields, Q. P. Unterreithmeier, N. P. de Leon, H. Park, and M. D. Lukin, Physical Review Letters **114**, 136402 (2015).
[9] L. Hacquebard and L. Childress, Physical Review A **97**, 063408 (2018).
[10] Y. Doi, T. Fukui, H. Kato, T. Makino, S. Yamasaki, T. Tashima, H. Morishita, S. Miwa, F. Jelezko, Y. Suzuki, *et al.*, Physical Review B **93**, 081203 (2016).